

pubs.acs.org/JACS Article

Domain-Specific Phase Transitions in a Supramolecular Nanostructure

Samuel J. Kaser, Ty Christoff-Tempesta, Linnaea D. Uliassi, Yukio Cho, and Julia H. Ortony*



Cite This: J. Am. Chem. Soc. 2022, 144, 17841–17847



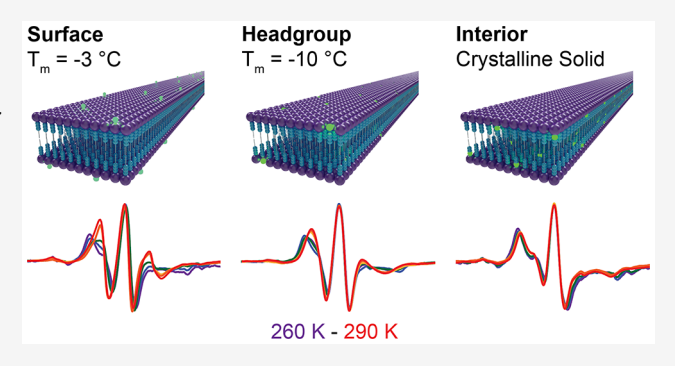
ACCESS I

III Metrics & More

Article Recommendations

SI Supporting Information

ABSTRACT: Understanding thermal phase behavior within nanomaterials can inform their rational design for medical technologies like drug delivery systems and vaccines, as well as for energy technologies and catalysis. This study resolves thermal phases of discrete domains within a supramolecular aramid amphiphile (AA) nanoribbon. Dynamics are characterized by X-band EPR spectroscopy of spin labels positioned at specific sites through the nanoribbon cross-section. The fitting of the electron paramagnetic resonance (EPR) line shapes reveals distinct conformational dynamics, with fastest dynamics at the surface water layer, intermediate dynamics within the flexible cationic head group domain, and slowest dynamics in the interior aramid domain.



Measurement of conformational mobility as a function of temperature reveals first- and second-order phase transitions, with melting transitions observed in the surface and head group domains and a temperature-insensitive crystalline phase in the aramid domain. Arrhenius analysis yields activation energies of diffusion at each site. This work demonstrates that distinct thermal phase behaviors between adjacent nanodomains within a supramolecular nanostructure may be resolved and illustrates the utility of EPR spectroscopy for thermal phase characterization of nanostructures.

■ INTRODUCTION

Self-assembly in water provides a convenient route to novel soft nanomaterials, $^{1-3}$ which have applications in tissue regeneration, 4 drug delivery, 5 and energy storage. Recently, extensive progress on self-assembled nanoparticles has been made for the delivery of vaccines and drugs. A hallmark feature of self-assembled materials is their multiple discrete internal domains, which exhibit nanoscale dimensions. In amphiphilic self-assembly, hydrophilic regions of the molecules reside at the aqueous interface, while hydrophobic regions of the molecules make up internal domains that are shielded from water. This organization yields nanostructures of molecular dimensions. The properties of each domain are controlled by their intermolecular forces, which can include hydrogen bonding, ionic bonding, and $\pi-\pi$ stacking, as well as more exotic interactions.

Many intricate and elegant examples of self-assembled materials with discrete internal nanoscale domains can be found in the literature, including liposome-DNA complexes, amphiphilic block copolymers, small molecule amphiphile nanostructures, and hybrid organic-inorganic micelles. Domains with distinct local chemistry will vary in their strength of intermolecular interactions and correspondingly in their thermal phase behavior. Domain-specific dynamics are likely to play an important role in nanostructures' mechanical stability, triggered or controlled release of cargo, and solute partitioning. However, it is challenging to

investigate domain-specific phase behavior due to the small dimensions and the close proximity of the adjacent domains.

Characterization of thermal phases within nanostructures requires sub-nanometer spatial resolution and high sensitivity to achieve the explicit assignment of phase transitions to a particular domain and also to resolve the phase behavior between adjacent domains. However, conventional phase characterization techniques often require high concentrations or solvent removal and are thus not practical for nanostructures in water with internal domains that occupy small volume fractions of the overall sample. Therefore, further investigation is needed to understand how interfacial behavior and enforced ordering affect phase transitions in nanostructured soft materials. ²⁹

In this work, aramid amphiphile (AA) nanoribbons are investigated as a model system for domain-specific phase behavior in a self-assembled nanostructure. AAs comprise a short hydrophobic tail, a Kevlar-inspired aromatic amide (aramid) backbone, and a hydrophilic charged head group.³⁰

Received: June 4, 2022 Published: September 20, 2022





AAs spontaneously self-assemble in water. The inclusion of the aramid domain leads to nanoribbons with extraordinary mechanical properties. Excellent spatial resolution is required to distinguish phase behavior in these adjacent nanodomains. However, very distinct thermal phase behavior is expected between different domains due to the differences in intermolecular interaction strengths: strong and anisotropic π - π stacking and hydrogen bonding dominate the backbone aramid domain, whereas the aliphatic head group is conformationally flexible.

Discussions of motion within nanomaterials invoke two distinct but related phenomena: molecular exchange, where individual molecules may exchange between neighboring nanostructures, and conformational dynamics, which describes the jiggling of a given molecule within a nanostructure.³¹ Exchange and cross-sectional conformational dynamics have been measured previously for peptide amphiphile (PA) nanofibers.²² In this case, the presence of slow, solid-like internal dynamics is correlated with the slower exchange. In comparison to PAs, the AA nanoribbon exhibits dramatically slower, unmeasurable exchange dynamics, 30 and therefore, we hypothesize that the aramid domain within AA nanoribbons will show dramatically slower conformational dynamics, too characteristic of a true solid-like crystal. We further hypothesize that the internal dynamics of AA nanoribbons will be temperature-insensitive, as intermolecular interactions between aramid domains are impervious to thermal fluctuations.

Surface and interior conformational dynamics can be characterized by site-directed spin labeling and electron paramagnetic resonance (SDSL-EPR) spectroscopy experiments.³² In SDSL-EPR, a spin label composed of a stable nitroxide radical is installed at a specific position within a macromolecule or supramolecular structure, and EPR spectroscopy is used to characterize conformational dynamics. Fast local dynamics result in isotropic averaging of the EPR signal, while slow dynamics produce a broadened anisotropic line shape. Motions in the order of nanoseconds to microseconds produce an intermediate spectrum with a line shape highly sensitive to conformational dynamics described by the rotational diffusion rate, $D_{\rm r}^{33}$ Spectra in this intermediate range can be fitted with a stochastic Liouville equation as implemented in the classic nonlinear least-squares stochastic Liouville (NLSL) program.³⁴ These fits may be carried out in batches via a chi-squared cluster analysis program (CSCA), 35 allowing us to determine local rotational diffusion rates to quantify conformational dynamics with sub-nanometer resolution. With this approach, differences in motional behavior can be identified between domains that may differ positionally by just a few bonds.

SDSL-EPR is widely applied in biophysical studies to probe protein structure, dynamics, and ligand binding events; ^{36–38} phospholipid membrane fluidity; ^{39,40} and sequence-localized differences in DNA rigidity. ⁴¹ Excellent spatial resolution afforded by SDSL-EPR allows for the explicit assignment of segments/regions in polyphasic materials to observed phase transitions, in contrast with conventional techniques for studying phase transitions like differential scanning calorimetry. SDSL-EPR has been used to show a constant glass transition temperature between the chain ends and the interior of polystyrene chains. ⁴² Moreover, SDSL-EPR is an *in situ* measurement technique, allowing conformational dynamics to

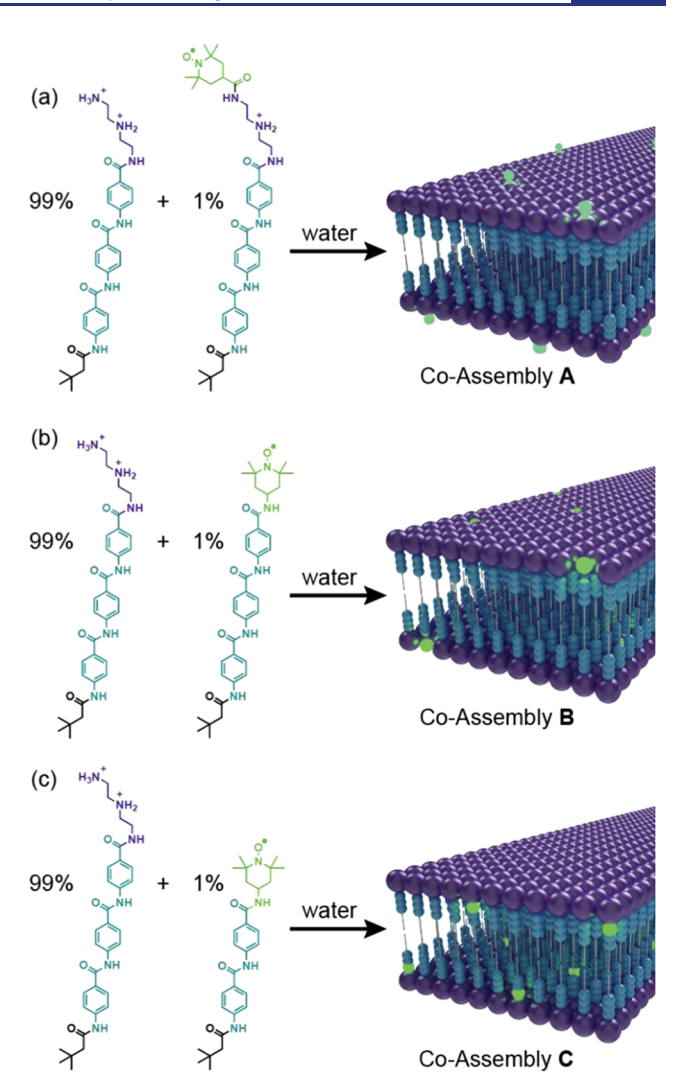


Figure 1. Self-assembly in the water of an aramid amphiphile (AA) with spin-labeled analogues yields nanoribbons with spin labels positioned at selected sites for EPR characterization. The purple balls represent charged surface groups, the teal balls represent the aramid domain, and the gray sticks represent the hydrocarbon tail. The glowing green balls represent stable nitroxide spin labels. (a) Canonical AA, compound 1, is co-assembled with compound 2, leading to a nanoribbon with the spin label above the surface (coassembly A). (b) Co-assembly of compound 1 with 3 leads to nanoribbons with spin labels embedded in the surface domain (coassembly B). (c) Co-assembly of compounds 1 and 4 leads to nanoribbons with spin labels in the aramid domain (co-assembly C). Nanoribbon schematics adapted from Biophys J., 119 (10), Lindemann W. R. et al., Global Minimization Toolkit for Batch-Fitting and χ^2 Cluster Analysis of CW-EPR Spectra, 1937–1945, Copyright (2020), with permission from Elsevier.

be measured under representative conditions for a given nanomaterial's desired application.

We synthesized AA molecules with radical electron spin labels positioned at three sites across the molecule. We coassembled each spin-labeled AA at low ratios with the prototypical AAs and measured temperature-dependent EPR spectra. This approach allows us to exploit the strong intermolecular interactions of aramid domains between both species to ensure aqueous co-assembly from evaporated organic solutions. These experiments were designed to probe

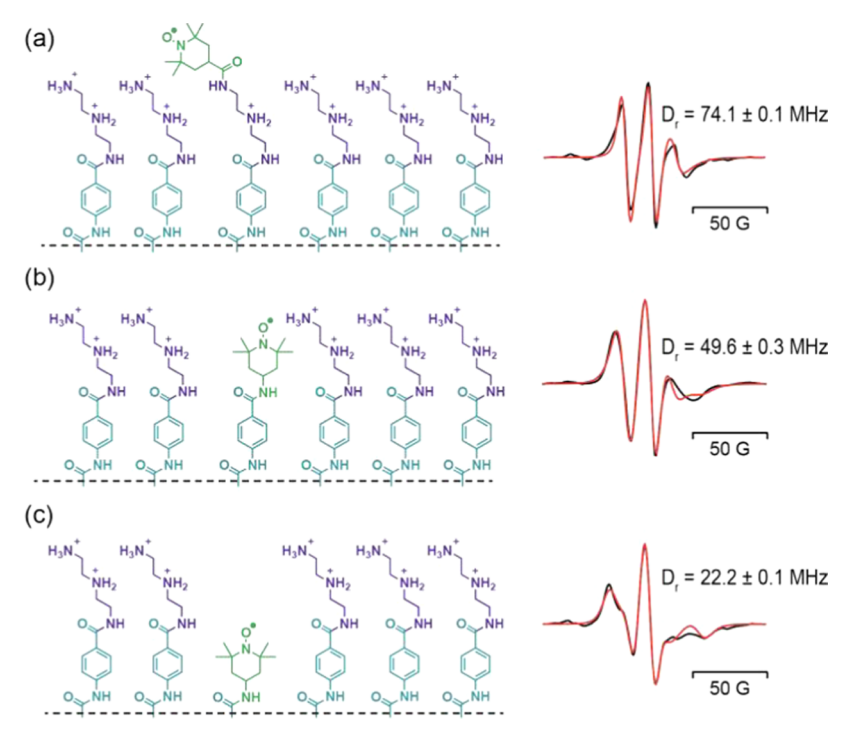


Figure 2. Depiction of the approximate spin label placement in co-assemblies and their room temperature X-band EPR spectra. Spectra (black) were measured for each co-assembly at 3315 G center field and fit with an NLSL-based MOMD simulation (red). Rotational diffusion rates D_r extracted from each simulated fit are reported next to each spectrum. Spin label position and corresponding EPR spectra are depicted with (a) spin labels above the nanoribbon surface, (b) spin labels in the head group domain, and (c) spin labels in the aramid domain.

the dynamics of individual domains within the assembly and to determine site-specific phase behavior.

■ RESULTS AND DISCUSSION

We prepared suspensions of AA nanoribbons by self-assembly in water. Each sample is composed of 99 mol % unlabeled AA (compound 1)³⁰ and 1% spin-labeled AA (Figure 1). Spin-labeled molecules of variable length were used to resolve domain-specific phase behavior, with compound 2 featuring 4-carboxyTEMPO coupled to the terminal head group nitrogen, compound 3 attaching 4-aminoTEMPO to the third aramid unit, and compound 4 attaching 4-aminoTEMPO to the second aramid unit (Figure 1). Nanoribbons of compound 1 spin-labeled with compounds 2, 3, and 4 were respectively designated A–C. Each co-assembly was imaged by transmission electron microscopy (TEM). In all cases, we verified that nanoribbon morphologies with consistent dimensions are observed (Figure S7).⁴³

The site-specific dynamics of each spin-labeled nanoribbon in aqueous suspension were assessed by EPR. The NLSL and CSCA programs were used to fit the spectra with a microscopic order-macroscopic disorder (MOMD) model, which describes the EPR spectra of nitroxyl radicals with local ordering in the slow-motion regime. The EPR spectra of all three co-assemblies were fit and are shown in Figure 2. EPR line shape fitting also provides rotational diffusion rates, D_{rp} which describe the spin label's conformational dynamics in its local environment. The line shapes in Figure 2 indicate that the spin labels reside in a slow-motion regime, and, therefore, the spin labels are intimately incorporated into the nanoribbons. The absence of exchange broadening confirms that the spin labels are dispersed throughout the nanoribbons, and the good quality of fits via the MOMD model and single-component

spectra confirm that the spin labels probe a uniform local environment.

The spin label positioned above the surface of the nanoribbon, as in co-assembly A, shows the fastest conformational dynamics with a rotational diffusion rate of 74.1 MHzconsistent with the spin label's expected placement between the flexible triazaheptane (TAH) surface and an adjacent water layer. The spin label within the head group layer (co-assembly B) shows intermediate dynamics, where the rotational diffusion rate is 49.6 MHz. This value is consistent with its placement in the ordered but flexible hydrophilic head group region. In contrast, the nanoribbon with spin labels in the aramid domain shows the slowest conformational dynamics, with a rotational diffusion rate of 22.2 MHz. To our surprise, the dynamics of co-assembly \boldsymbol{C} remain above the threshold for solid-like dynamics (~10 MHz).²² We attribute this elevated rotational diffusion rate to the spin label's position near the aramid-TAH interface, with TAH conferring some additional dynamic motion to the spin label's intermolecular environ-

Conformational dynamics were measured at variable temperature by X-band EPR spectroscopy to characterize domain-specific thermal phase behavior. EPR spectra were measured between 250 and 296 K for each co-assembly, and $D_{\rm r}$ values were determined at each temperature by CSCA (Figure 3). Extracted $D_{\rm r}$ values were verified by replicating measurements of each system at each temperature point above 273 K.

The variable temperature EPR spectra shown in Figure 3 show the thermal phase behavior at the spin label sites in each co-assembly, A–C. When the spin label is positioned above the nanoribbon surface, as in co-assembly A, a thermal phase transition is observed at 272 K, similar to that of bulk water. The other co-assemblies, B and C, with spin labels positioned in the head group domain and the aramid domain, respectively,

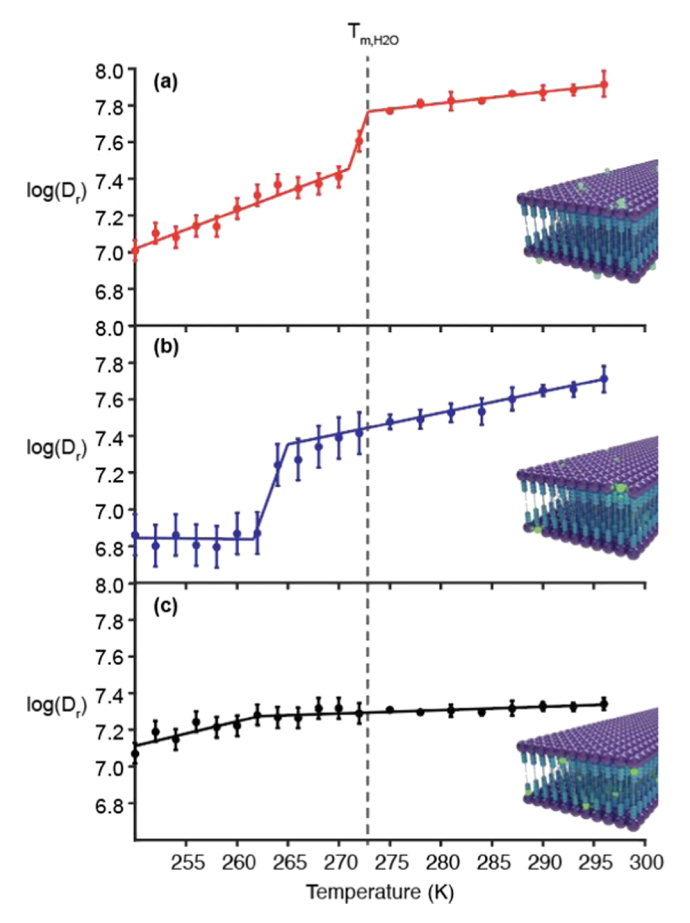


Figure 3. Site-specific thermal phase behavior within an AA nanoribbon determined by variable temperature X-band EPR. Rotational diffusion coefficients, $\log(D_{\rm f})$ (also known as rbar), plotted as a function of temperature for (a) an AA nanoribbon ensemble with spin labels above the surface (co-assembly A), (b) nanoribbons with spin labels in the head group domain (co-assembly B), and (c) nanoribbons with spin labels in the aramid domain (co-assembly C). The bulk melting temperature of water $(T_{\rm m,H_2O})$ is labeled with a vertical dashed line. Trend lines and error bars are determined as described in the Supporting Information. Nanoribbon schematics adapted from Biophys J., 119 (10), Lindemann W. R. et al., Global Minimization Toolkit for Batch-Fitting and χ^2 Cluster Analysis of CW–EPR Spectra, 1937–1945, Copyright (2020), with permission from Elsevier.

show no detectable discontinuity, i.e., phase transition, near 273 K. Despite the observed phase transition, the dynamics of the spin label above the nanoribbon surface (co-assembly A) remain faster than that of a spin label in a solid environment. Co-assembly B, by contrast, shows a consistent increase in dynamics from 264 to 296 K, suggesting that the freezing of water does not affect head group dynamics. With this spin label, a sharp drop to solid-like dynamics ($log(D_r) < 7$) is observed at 263 K. This first-order discontinuity implies that the head group domain undergoes a liquid-to-solid transition at that temperature. It is notable, then, that co-assembly A has no detectable discontinuity around 263 K, suggesting a distinct interfacial phase that remains liquid-like below the freezing temperature of both bulk water and that of the surface domain. Like co-assembly B, co-assembly C shows no phase transition at 273 K; instead, a phase transition is observed at 263 K. These results suggest that the spin label environment at the aramid domain is isolated from the bulk water but affected by

the dynamic motion of the head group domain. However, the phase transition near 263 K in the aramid domain is second-order, suggesting an interfacial local environment. The observation of this second-order phase transition supports our earlier suggestion that the local spin label environment of co-assembly C is influenced by the adjacent head group domain rather than being entirely isolated within the aramid domain.

The dynamics illustrated in Figure 3 describe thermal phase transitions as previously discussed but also contain information about the effect of temperature on molecular motion within each phase of each spin label environment. We carried out Arrhenius analysis of the variable temperature EPR above 273 K to determine activation energies of diffusion ($E_{\rm AD}$).

Figure 4 shows calculated $E_{\rm AD}$ values determined at each spin label site corresponding to Co-assemblies A–C. Each spin

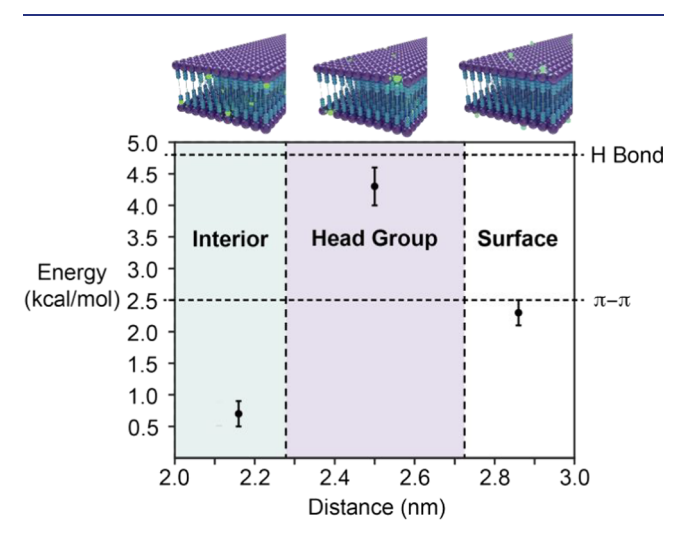


Figure 4. Activation energies of diffusion $(E_{\rm AD})$ of spin labels at specific sites of an aramid amphiphile nanoribbon. Activation energies of diffusion $(E_{\rm AD})$ are determined by Arrhenius analysis of EPR rotational diffusion rates between 275 and 293 K. $E_{\rm AD}$ values are plotted as a function of the distance of the nitroxyl N atom from the hydrocarbon tail. The aramid domain, head group domain, and surface water are shown in teal, purple, and white, respectively. Error bars are calculated from the Arrhenius plot slope error (Figure S28). Literature values for the β-sheet hydrogen bond and slipped parallel benzene π - π interaction strengths are labeled on the energy axis. A3,44 Nanoribbon schematics adapted from Biophys J., 119 (10), Lindemann W. R. et al., Global Minimization Toolkit for Batch-Fitting and χ^2 Cluster Analysis of CW-EPR Spectra, 1937–1945, Copyright (2020), with permission from Elsevier.

label site is represented by an estimated distance from the hydrophobic hydrocarbon domain. The $E_{\rm AD}$ in the aramid domain (co-assembly C) is 0.7 \pm 0.2 kcal/mol, which is substantially less than the estimated energy of a single $\pi-\pi$ interaction or amide hydrogen bond between aramid units. If the motion of the spin label did, in fact, reflect the conformational motion of the aramid units, the calculated $E_{\rm AD}$ should be at a higher order of magnitude (perhaps tens of kcal/mol), corresponding to the disruption of numerous interdomain hydrogen bonds and $\pi-\pi$ interactions. Thus, the observed conformational motion of the spin label in the aramid domain is not capable of disrupting interactions between neighboring aramid units. Instead, the dynamics observed by EPR may be attributed to spin label motion within a confined pocket since both the rotational diffusion rate and the activation energy of diffusion are relatively low. Nitroxide EPR spectral line shapes are highly sensitive to the intermediate time scale conformational motion characteristic of ordered/viscous liquids and flexible polymer chains and can be influenced by these rotations even if they are of low amplitude. Therefore, the aramid domain is likely a solid-like environment despite the EPR spectra of co-assembly C showing slightly faster conformational dynamics than are typical for a bulk solid.

As shown in Figure 4, when the spin label is positioned in the head group domain (co-assembly B), $E_{\rm AD}$ is found to be 4.3 \pm 0.3 kcal/mol, roughly 6 times greater than that of the aramid domain. This value is comparable to a strong intermolecular interaction, such as a hydrogen bond. This energy barrier is consistent with conformational dynamics in this domain, displacing amine groups in the triazaheptane head groups.

The $E_{\rm AD}$ obtained when the spin label is in the surface water shows an intermediate value of 2.3 \pm 0.2 kcal/mol. This activation energy value is consistent with motion that affects intermolecular interactions of neighboring groups or molecules to a modest extent, i.e., the displacement of liquid water molecules that maintain a dynamic hydrogen bonding network.

CONCLUSIONS

In this work, we used EPR spectroscopy, along with site-directed spin labeling (SDSL), to characterize the dynamics and phase behavior of an aramid amphiphile (AA) supramolecular nanostructure with domain specificity. We showed that by performing variable temperature EPR spectroscopy, we can detect thermal phase transitions in confined domains within the nanostructure. In particular, melting transitions below room temperature are observed in the surface water and head group domains but not in the aramid domain. A flexible, liquid-like environment was identified at the surface of the AA nanoribbon. These results indicate that the highly mechanically stable AA nanostructure surface is kinetically suited for applications in catalysis, substrate binding, and partitioning of hydrophilic/charged substances from an aqueous environment

We calculated activation energies of diffusion (E_{AD}) from Arrhenius analysis of the variable temperature EPR spectra and demonstrated the importance of understanding $E_{\rm AD}$ values in supramolecular systems. The $E_{\rm AD}$ values obtained when the spin label is in the head group and surface domains reflect the energy required to disrupt the local intermolecular interactions. In contrast, the $E_{\rm AD}$ of the spin label in the aramid domain is substantially lower than in the head group and surface domains, even though the dominant local intermolecular interaction of the aramid domain is strong hydrogen bonding. This discrepancy is understood by recognizing that the aramid domain is truly solid-like, and consequently local diffusion, even upon heating, is incapable of disrupting the intermolecular hydrogen bonds. Thus, this work capitalizes on the unique phase behavior of the nanoribbon's aramid domain to demonstrate that Arrhenius analysis can be used to identify crystalline solid-like domains.

Further, this work provides a tool for the analysis of thermal phase transitions of nanoscale domains within supramolecular materials. This capability will enable the development of rational design principles for diverse self-assembled nanomaterials in the future.

ASSOCIATED CONTENT

Supporting Information

The Supporting Information is available free of charge at https://pubs.acs.org/doi/10.1021/jacs.2c05908.

Materials and methods, synthesis and characterization of spin labels, sample EPR spectra and corresponding fit outputs, and additional data tabulation and analysis (PDF)

AUTHOR INFORMATION

Corresponding Author

Julia H. Ortony — Department of Materials Science and Engineering, Massachusetts Institute of Technology, Cambridge, Massachusetts 02139, United States; orcid.org/0000-0001-7446-6207; Email: ortony@mit.edu

Authors

Samuel J. Kaser — Department of Chemistry, Massachusetts Institute of Technology, Cambridge, Massachusetts 02139, United States; © orcid.org/0000-0002-1743-5612

Ty Christoff-Tempesta – Department of Materials Science and Engineering, Massachusetts Institute of Technology, Cambridge, Massachusetts 02139, United States

Linnaea D. Uliassi — Department of Materials Science and Engineering, Massachusetts Institute of Technology, Cambridge, Massachusetts 02139, United States

Yukio Cho – Department of Materials Science and Engineering, Massachusetts Institute of Technology, Cambridge, Massachusetts 02139, United States

Complete contact information is available at: https://pubs.acs.org/10.1021/jacs.2c05908

Author Contributions

The manuscript was written with the contributions of all authors. All authors have given approval to the final version of the manuscript.

Funding

This material is based upon the work supported by the National Science Foundation under Grant No. CHE-1945500. T.C-.T. acknowledges the support of the Hugh Hampton Young Fellowship. S.K. acknowledges the support of the Natural Sciences and Engineering Research Council of Canada's postgraduate scholarship (PGS-D).

Notes

The authors declare no competing financial interest.

ACKNOWLEDGMENTS

We thank Ryan Allen for creating the nanoribbon images shown in Figures 1, 3, and 4. We thank John Grimes for helping with the operation of the MIT Department of Chemistry Instrumentation Facility (DCIF) EPR spectrometer. This work made use of the MRSEC Shared Experimental Facilities at MIT, supported by the National Science Foundation under award number DMR-14-19807 and the MIT DCIF.

ABBREVIATIONS

AA aramid amphiphile
CSCA chi-squared cluster analysis
EPR electron paramagnetic resonance

NLSL nonlinear least-squares stochastic Liouville PA peptide amphiphile SDSL-EPR site-directed spin label EPR

REFERENCES

- (1) Aida, T.; Meijer, E. W.; Stupp, S. I. Functional supramolecular polymers. *Science* **2012**, *335*, 813–817.
- (2) Lehn, J.-M. Supramolecular Chemistry: Receptors, Catalysts, and Carriers. *Science* **1985**, 227, 849–856.
- (3) Whitesides, G. M.; Mathias, J. P.; Seto, C. T. Molecular Self-Assembly and Nanochemistry: a Chemical Strategy for the Synthesis of Nanostructures. *Science* **1991**, *254*, 1312–1319.
- (4) Silva, G. A.; Czeisler, C.; Niece, K. L.; Beniash, E.; Harrington, D. A.; Kessler, J. A.; Stupp, S. I. Selective Differentiation of Neural Progenitor Cells by High-Epitope Density Nanofibers. *Science* **2004**, 303, 1352–1355.
- (5) Yadav, S.; Sharma, A. K.; Kumar, P. Nanoscale Self-Assembly for Therapeutic Delivery. Front. Bioeng. Biotechnol. 2020, 8, 1–24.
- (6) Xiu, Y.; Zhang, X.; Feng, Y.; Wei, R.; Wang, S.; Xia, Y.; Cao, M.; Wang, S. Peptide-mediated porphyrin based hierarchical complexes for light-to-chemical conversion. *Nanoscale* **2020**, *12*, 15201–15208.
- (7) Mitchell, M. J.; Billingsley, M. M.; Haley, R. M.; Wechsler, M. E.; Peppas, N. A.; Langer, R. Engineering precision nanoparticles for drug delivery. *Nat. Rev. Drug Discovery* **2021**, *20*, 101–124.
- (8) Sijbesma, R. P.; Meijer, E. W. Self-assembly of well-defined structures by hydrogen bonding. *Curr. Opin. Colloid Interface Sci.* 1999, 4, 24–32.
- (9) Faul, C. F. J. Ionic Self-Assembly for Functional Hierarchical Nanostructured Materials. *Acc. Chem. Res.* **2014**, *47*, 3428–3438.
- (10) Lübtow, M.; Helmers, I.; Stepanenko, V.; Albuquerque, R. Q.; Marder, T. B.; Fernández, G. Self-Assembly of 9,10-Bis-(phenylethynyl) Anthracene (BPEA) Derivatives: Influence of π - π and Hydrogen-Bonding Interactions on Aggregate Morphology and Self-Assembly Mechanism. *Chem. Eur. J.* **2017**, 23, 6198–6205.
- (11) Strassert, C. A.; Chien, C.-H.; GalvezLopez, M. D.; Kourkoulos, D.; Hertel, D.; Meerholz, K.; DeCola, L. Switching On Luminescence by the Self-Assembly of a Platinum(II) Complex into Gelating Nanofibers and Electroluminescent Films. *Angew. Chem., Int. Ed.* **2011**, *50*, 946–950.
- (12) Ryan, D. M.; Doran, T. M.; Nilsson, B. L. Complementary $\pi \pi$ Interactions Induce Multicomponent Coassembly into Functional Fibrils. *Langmuir* **2011**, *27*, 11145–11156.
- (13) Tuo, D.-H.; Liu, W.; Wang, X.-Y.; Wang, X.-D.; Ao, Y.-F.; Wang, Q.-Q.; Li, Z.-Y.; Wang, D.-X. Toward Anion— π Interactions Directed Self-Assembly with Predesigned Dual Macrocyclic Receptors and Dianions. *J. Am. Chem. Soc.* **2019**, *141*, 1118—1125.
- (14) Rädler, J. O.; Koltover, I.; Salditt, T.; Safinya, C. R. Structure of DNA-Cationic Liposome Complexes: DNA Intercalation in Multi-lamellar Membranes in Distinct Interhelical Packing Regimes. *Science* 1997, 275, 810–814.
- (15) Jhaveri, A. M.; Torchilin, V. P. Multifunctional polymeric micelles for delivery of drugs and siRNA. *Front. Pharmacol.* **2014**, *5*, 1–26.
- (16) Elabd, Y. A.; Hickner, M. A. Block Copolymers for Fuel Cells. *Macromolecules* **2011**, *44*, 1–11.
- (17) Rösler, A.; Vandermeulen, G. W. M.; Klok, H.-A. Advanced drug delivery devices via self-assembly of amphiphilic block copolymers. *Adv. Drug Delivery Rev.* **2012**, *64*, 270–279.
- (18) Strauss, M. J.; Hwang, I.; Evans, A. M.; Natraj, A.; Aguilar-Enriquez, X.; Castano, I.; Roesner, E. K.; Choi, J. W.; Dichtel, W. R. Lithium-Conducting Self-Assembled Organic Nanotubes. *J. Am. Chem. Soc.* **2021**, *143*, 17655–17665.
- (19) Cui, H.; Webber, M. J.; Stupp, S. I. Self-assembly of peptide amphiphiles: from molecules to nanostructures to biomaterials. *Biopolymers* **2010**, *94*, 1–18.
- (20) Wu, Y.; Shah Darshil, U.; Liu, C.; Yu, Z.; Liu, J.; Ren, X.; Rowland Matthew, J.; Abell, C.; Ramage Michael, H.; Scherman Oren, A. Bioinspired supramolecular fibers drawn from a multiphase

- self-assembled hydrogel. Proc. Natl. Acad. Sci. U.S.A. 2017, 114, 8163-8168.
- (21) Zeng, M.; Chen, K.; Tan, J.; Zhang, J.; Wei, Y. A Supramolecular Catalyst Self-Assembled From Polyoxometalates and Cationic Pillar[5] arenes for the Room Temperature Oxidation of Aldehydes. *Front. Chem.* **2018**, *6*, 1–8.
- (22) Ortony, J. H.; Newcomb, C. J.; Matson, J. B.; Palmer, L. C.; Doan, P. E.; Hoffman, B. M.; Stupp, S. I. Internal dynamics of a supramolecular nanofibre. *Nat. Mater.* **2014**, *13*, 812–816.
- (23) Schief, W. R.; Touryan, L.; Hall, S. B.; Vogel, V. Nanoscale Topographic Instabilities of a Phospholipid Monolayer. *J. Phys. Chem. B* **2000**, *104*, 7388–7393.
- (24) Guerrini, G.; Magrì, D.; Gioria, S.; Medaglini, D.; Calzolai, L. Characterization of nanoparticles-based vaccines for COVID-19. *Nat. Nanotechnol.* **2022**, *17*, 570–576.
- (25) Newcomb, C. J.; Sur, S.; Ortony, J. H.; Lee, O.-S.; Matson, J. B.; Boekhoven, J.; Yu, J. M.; Schatz, G. C.; Stupp, S. I. Cell death versus cell survival instructed by supramolecular cohesion of nanostructures. *Nat. Commun.* **2014**, *5*, No. 3321.
- (26) Forrey, C.; Douglas, J. F.; Gilson, M. K. The fundamental role of flexibility on the strength of molecular binding. *Soft Matter* **2012**, *8*, 6385–6392.
- (27) Munoz, S.; Greenbaum, S. Review of Recent Nuclear Magnetic Resonance Studies of Ion Transport in Polymer Electrolytes. *Membranes* **2018**, *8*, 1–23.
- (28) Wang, X.; Zeng, T.; Nourrein, M.; Lai, B.-H.; Shen, K.; Wang, C.-L.; Sun, B.; Zhu, M. Concentration-dependent self-assembly structures of an amphiphilic perylene diimide with tri(ethylene glycol) substituents at bay positions. *RSC Adv.* **2017**, *7*, 26074–26081.
- (29) Tantakitti, F.; Boekhoven, J.; Wang, X.; Kazantsev, R. V.; Yu, T.; Li, J.; Zhuang, E.; Zandi, R.; Ortony, J. H.; Newcomb, C. J.; Palmer, L. C.; Shekhawat, G. S.; de la Cruz, M. O.; Schatz, G. C.; Stupp, S. I. Energy landscapes and functions of supramolecular systems. *Nat. Mater.* **2016**, *15*, 469–476.
- (30) Christoff-Tempesta, T.; Cho, Y.; Kim, D.-Y.; Geri, M.; Lamour, G.; Lew, A. J.; Zuo, X.; Lindemann, W. R.; Ortony, J. H. Self-assembly of aramid amphiphiles into ultra-stable nanoribbons and aligned nanoribbon threads. *Nat. Nanotechnol.* **2021**, *16*, 447–454.
- (31) Cho, Y.; Christoff-Tempesta, T.; Kaser, S. J.; Ortony, J. H. Dynamics in supramolecular nanomaterials. *Soft Matter* **2021**, *17*, 5850–5863.
- (32) Fleissner, M. R.; Bridges, M. D.; Brooks, E. K.; Cascio, D.; Kálai, T.; Hideg, K.; Hubbell, W. L. Structure and dynamics of a conformationally constrained nitroxide side chain and applications in EPR spectroscopy. *Proc. Natl. Acad. Sci. U.S.A.* **2011**, *108*, 16241–16246.
- (33) Jeschke, G. Conformational dynamics and distribution of nitroxide spin labels. *Prog. Nucl. Magn. Reson. Spectrosc.* **2013**, 72, 42–60.
- (34) Budil, D. E.; Lee, S.; Saxena, S.; Freed, J. H. Nonlinear-Least-Squares Analysis of Slow-Motion EPR Spectra in One and Two Dimensions Using a Modified Levenberg—Marquardt Algorithm. *J. Magn. Reson., Ser. A* **1996**, *120*, 155–189.
- (35) Lindemann, W. R.; Christoff-Tempesta, T.; Ortony, J. H. A Global Minimization Toolkit for Batch-Fitting and χ^2 Cluster Analysis of CW-EPR Spectra. *Biophys. J.* **2020**, *119*, 1937–1945.
- (36) Lindemann, W. R.; Mijalis, A. J.; Alonso, J. L.; Borbat, P. P.; Freed, J. H.; Arnaout, M. A.; Pentelute, B. L.; Ortony, J. H. Conformational Dynamics in Extended RGD-Containing Peptides. *Biomacromolecules* **2020**, *21*, 2786–2794.
- (37) Torricella, F.; Pierro, A.; Mileo, E.; Belle, V.; Bonucci, A. Nitroxide spin labels and EPR spectroscopy: A powerful association for protein dynamics studies. *Biochim. Biophys. Acta, Proteins Proteomics* **2021**, *1869*, No. 140653.
- (38) Klug, C. S.; Feix, J. B.Methods and Applications of Site-Directed Spin Labeling EPR Spectroscopy. In *Methods Cell Biology*; Academic Press, 2008; Vol. 84, pp 617–658.

- (39) Lyles, D. S.; Landsberger, F. R. Sendai virus-induced hemolysis: reduction in heterogeneity of erythrocyte lipid bilayer fluidity. *Proc. Nalt. Acad. Sci. U.S.A.* 1977, 74, 1918–1922.
- (40) Catte, A.; White, G. F.; Wilson, M. R.; Oganesyan, V. S. Direct Prediction of EPR Spectra from Lipid Bilayers: Understanding Structure and Dynamics in Biological Membranes. *ChemPhysChem* **2018**, *19*, 2183–2193.
- (41) Popova, A. M.; Kálai, T.; Hideg, K.; Qin, P. Z. Site-Specific DNA Structural and Dynamic Features Revealed by Nucleotide-Independent Nitroxide Probes. *Biochemistry* **2009**, *48*, 8540–8550.
- (42) Miwa, Y.; Urakawa, O.; Doi, A.; Yamamoto, K.; Nobukawa, S. Glass Transition Temperature and β Relaxation Temperature around Chain End of Polystyrene Determined by Site Specific Spin Labeling. *J. Phys. Chem. B* **2012**, *116*, 1282–1288.
- (43) Kaser, S. J.; Lew, A. J.; Kim, D.-Y.; Christoff-Tempesta, T.; Cho, Y.; Ortony, J. H. Effects of molecular flexibility and head group repulsion on aramid amphiphile self-assembly. *Mol. Syst. Des. Eng.* **2021**, *6*, 1016–1024.
- (44) Sheu, S. Y.; Yang, D. Y.; Selzle, H. L.; Schlag, E. W. Energetics of hydrogen bonds in peptides. *Proc. Natl. Acad. Sci. U.S.A.* **2003**, *100*, 12683–12687.
- (45) Tsuzuki, S.; Honda, K.; Uchimaru, T.; Mikami, M.; Tanabe, K. Origin of Attraction and Directionality of the π/π Interaction: Model Chemistry Calculations of Benzene Dimer Interaction. *J. Am. Chem. Soc.* **2002**, *124*, 104–112.

NOTE ADDED AFTER ASAP PUBLICATION

This paper was published on September 20, 2022. Two images in the Abstract graphic were transposed. This has been updated and the revised version was re-posted on September 23, 2022.

☐ Recommended by ACS

Morphological Transitions of a Photoswitchable Aramid Amphiphile Nanostructure

Dae-Yoon Kim, Julia H. Ortony, et al.

MARCH 18, 2021 NANO LETTERS

READ 🗹

Crescent-Shaped Supramolecular Tetrapeptide Nanostructures

Yin Wang, John B. Matson, et al.

NOVEMBER 13, 2020

JOURNAL OF THE AMERICAN CHEMICAL SOCIETY

READ 🗹

Supramolecular Copolymers of Peptides and Lipidated Peptides and Their Therapeutic Potential

Ruomeng Qiu, Samuel I. Stupp, et al.

MARCH 17, 2022

JOURNAL OF THE AMERICAN CHEMICAL SOCIETY

READ 🗹

Crystallization of Precise Side-Chain Giant Molecules with Tunable Sequences and Functionalities

Fengfeng Feng, Hao Liu, et al.

NOVEMBER 24, 2021

MACROMOLECULES

READ **C**

Get More Suggestions >